https://doi.org/10.1007/s11467-023-1360-9

RESEARCH ARTICLE

Curved anisotropic polaritons

Tao Hou[1,*], Yixiao Ge[1,*], Shuwen Xue[1], Huanyang Chen[1,2,†]

[1] Department of Physics and Institute of Electromagnetics and Acoustics, Xiamen University, Xiamen 361005, China

[2] Jiujiang Research Institute of Xiamen University, Jiujiang 332000, China

[*]These authors contributed equally to this work.

Corresponding author. E-mail: [†]kenyon@xmu.edu.cn

Received August 2, 2023; accepted October 12, 2023

Supporting Information

Contents

Section 1: The calculation of the geodesics

In this paper, we consider the two-dimensional geodesic equation:

$$\frac{d^2x^\lambda}{dt^2}+\Gamma^\lambda_{uv}\frac{dx^u}{dt}\frac{dx^v}{dt}=0. \tag{S1}$$

According to the anisotropic two-dimensional radial metric

$$ds^2=M(\frac{2}{\rho^2+1})^2d\rho^2+N(\frac{2\rho}{\rho^2+1})^2d\varphi^2, \tag{S2}$$

the corresponding metric coefficient can be obtained,

$$\boldsymbol{g}=\begin{bmatrix} M(\frac{2}{\rho^2+1})^2 & 0 \\ 0 & N(\frac{2\rho}{\rho^2+1})^2 \end{bmatrix}. \tag{S3}$$

By substituting Eq. (S3) into Eq. (S1), the coupled equations of motion in polar coordinates can be obtained

$$\ddot{\rho}+\frac{1}{2g_{11}}\frac{\partial g_{11}}{\partial \rho}\dot{\rho}^2-\frac{1}{2g_{11}}\frac{\partial g_{22}}{\partial \rho}\dot{\varphi}^2=0,$$
$$\ddot{\varphi}+\frac{1}{g_{22}}\frac{\partial g_{22}}{\partial \rho}\dot{\rho}\dot{\varphi}=0, \tag{S4}$$

where "." stands for $\partial/\partial t$. By solving Eq. (S4), we can obtain the geodesics on the anisotropic plane.

After a suitable choice of orthonormal coordinate (θ, φ), the line element can be further written in a diagonal form as $ds^2=\tilde{g}_{11}d\theta d\theta+2\tilde{g}_{12}d\theta d\varphi+\tilde{g}_{22}d\varphi d\varphi$, by a coordinate transformation $(\theta,\varphi)=[\theta(\rho,\varphi),\varphi(\rho,\varphi)]$. A conformal structure is an equivalence class of metrics that differs by the area scaling. We need to point out that surfaces with conformally equivalent metrics are totally different geometrical objects if we consider their physical properties. However, one can always find a conformal mapping between two different surfaces, where the angle is preserved. In previous studies, the spherical geodesic geometry is proved to be equivalent to the planar Maxwell fisheye metric. Similarly, the anisotropic Maxwell fish-eye line element is equivalent to an anisotropic sphere surface by an inverse projection of light (see Fig. 1(b) in the main text):

$$ds^2=M(\frac{2}{\rho^2+1})^2d\rho^2+N(\frac{2\rho}{\rho^2+1})^2d\varphi^2=Md\theta^2+N\sin^2\theta d\varphi^2. \tag{S5}$$

The corresponding metric coefficient can be obtained.

$$\boldsymbol{g}=\begin{bmatrix}M & 0\\ 0 & N\sin^2\theta\end{bmatrix}. \tag{S6}$$

In this case, the geodesic trajectory on the non-European plane corresponds to the ray trajectory on the anisotropic sphere. By substituting Eq. (S6) into the geodesic Eq. (S1) with spherical coordinate system (θ, φ), we obtain the coupled equations of motion in spherical surface coordinate:

$$\ddot{\theta}-\frac{N}{M}\sin\theta\cos\theta\dot{\varphi}^2=0, \tag{S7a}$$
$$\ddot{\varphi}+\frac{2\cos\theta}{\sin\theta}\dot{\theta}\dot{\varphi}=0. \tag{S7b}$$

By solving the Eq. (S7), we can obtain the geodesics on the spherical surface.

Section 2: Equivalent potential energy analysis

Multiplying Eq. (S7b) by $\sin^2\theta$, we obtain

$$\sin^2\theta\ddot{\varphi}+2\cos\theta\sin\theta\dot{\theta}\dot{\varphi}=\frac{d(\sin^2\theta\dot{\varphi})}{dt}=0, \tag{S8}$$

which implies that

$$\alpha^2\sin^2\theta\dot{\varphi}=L. \tag{S9}$$

A similar treatment for the Eq. (S7a) yields

$$\frac{\dot{\theta}^2}{2}+\frac{L^2}{2\alpha^2\sin^2\theta}=E. \tag{S10}$$

Here, the integral constants L and E are the angular momentum and energy of the system [S1], respectively. From the kinetic energy $\frac{\dot{\theta}^2}{2}$ in Eq. (S10), the photon can be regarded as a charged particle, while the effective potential is a

function of the azimuth angle $V(\theta)=\frac{L^2}{2\alpha^2\sin^2\theta}$. Refer to the treatment of radial anisotropy cases [S2], we separate the rotational energy from the potential according to

$$V'(\theta)=\frac{L^2}{2\sin^2\theta}+V(\theta), \tag{S11}$$

where $L^2/2\sin^2\theta$ is the rotational energy of the point particle appearing in sphere coordinates [S3], and the real potential $V(\theta)$ is thus given by

$$V(\theta)=\frac{1-\alpha^2}{\alpha^2}\frac{L^2}{2\sin^2\theta}. \tag{S12}$$

These equations indicate that the motion of a light beam due to radial anisotropy is similar to the orbital motion under Coriolis force. Obviously, the potential can be attractive or repulsive, depending on the value of α^2. For the hyperbolic case $\alpha^2 < 0$, the potential is negative, which represents an attractive potential for the test photon. For the elliptical case: if $0 <\alpha^2< 1$, the potential is still attractive. Now the metric tensor describes the geometry of a hyperbolic cone that corresponds to a negative curvature singularity. If $\alpha^2>1$, the potential is repulsive, which corresponds to an ordinary conic geometry. Consequently, we can define the following topological charge [S2]

$$Q=\frac{1-\alpha^2}{\alpha^2}. \tag{S13}$$

From this topological charge, we can judge the symbol of curvature and potential energy for the elliptic/hyperbolic case according to the value of α.

Section 3: Equivalent refractive index profiles analysis

Firstly, we equivalent the anisotropic curved surface to the isotropic polar coordinate system,

$$ds^2=Md\theta^2+N\sin^2\theta d\varphi^2=n^2(d\rho^2+\rho^2d\varphi^2). \tag{S14}$$

According to the above equivalence relation, we can obtain:

$$\sqrt{M}\,d\theta=nd\rho, n\rho=\sqrt{N}\sin\theta. \tag{S15}$$

To solve the Eq. (S16) simultaneously, we can obtain

$$\theta=2\,\mathrm{Arctan}(\rho^{\sqrt{\frac{M}{N}}}). \tag{S16}$$

By substituting it back into the Eq. (S11), the refraction index of the map can be obtained

$$n=\frac{2\sqrt{N}\rho^{-1+\sqrt{\frac{N}{M}}}}{1+\rho^{2\sqrt{\frac{N}{M}}}}. \tag{S17}$$

The refraction index profile corresponds to a generalized Maxwell's fish-eye lens and α is the scaling parameter (Ref. [53] in the main text). When M=N=1, the corresponding refractive index distribution is Maxwell fish-eye lens, which also verifies the equivalence between the spherical surface and the fisheye plane. When $M\neq N$, the refractive index distribution reaches its maximum value at ρ=0 (M>N) and ρ=1 (M<N), respectively.

When we consider the hyperbolic metric (taking M<0, N>0 for example), Eq. (S14) can be rewritten as:

$$ds^2=-|M|d\theta^2+N\sin^2\theta d\phi^2=n^2(d\rho^2+\rho^2d\phi^2). \tag{S18}$$

Similarly, the equivalent refractive index of hyperbolic surface is

$$n=\frac{2\sqrt{N}\rho^{-1+i\sqrt{\frac{N}{|M|}}}}{1+\rho^{2i\sqrt{\frac{N}{|M|}}}}. \tag{S19}$$

Now the equivalent refractive index profile becomes a complex number. In order to explore the relationship between equivalent refractive index profiles $|n|$ and radius ρ, we draw it in the Fig. S1 below:

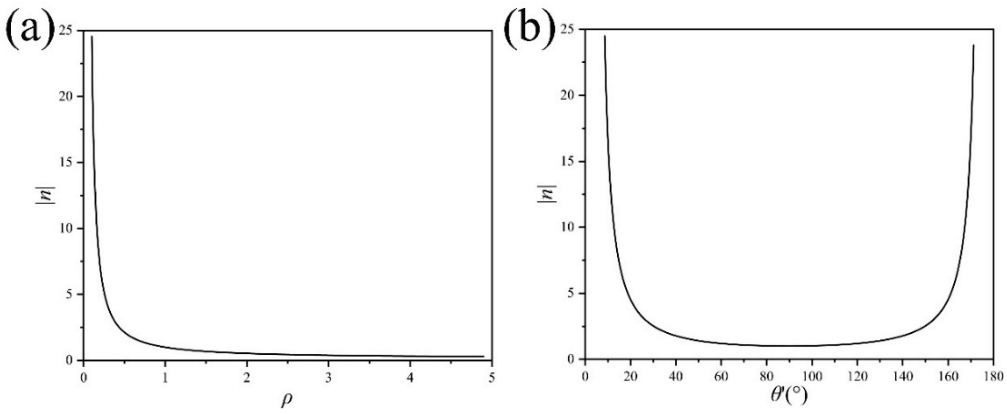

Fig. S1 (a) The relationship between equivalent refractive index profiles $|n|$ and radius ρ when M=-4 and N=1. **(b)** The relationship between equivalent refractive index profiles $|n|$ and azimuth angle θ' when M=-4 and N=1.

As shown in Fig. S1(a), we can find that the equivalent refractive index profiles at ρ=0 and ρ=∞ are infinite (similar to an artificial black hole) and 0 respectively. From the plane point of view, the light along the inner direction of the circle will be caught into the center, just like the optical black hole effect [S4]. In addition, when ρ is greater than 1, the refractive index changes more and more slowly with the increase of radius ρ, i.e., the refraction of light becomes weaker. As a result, light will eventually escape the center of the circle in parallel.

Then we equivalent the hyperbolic curved surface to an isotropic gradient index sphere,

$$ds^2=-|M|d\theta^2+N\sin^2\theta d\varphi^2=n^2(d\theta'^2+\sin^2\theta' d\varphi)\ . \tag{S20}$$

Similarly, we can obtain

$$-\sqrt{|M|}d\theta=nd\theta',\sqrt{N}\sin\theta=n\sin\theta'. \tag{S21}$$

Now, the refraction index of the map is

$$n=\frac{2\sqrt{N}\,\mathrm{Csc}(\theta')\,\mathrm{Tan}^{i\sqrt{\frac{N}{|M|}}}(\frac{\theta'}{2})}{1+\mathrm{Tan}^{2i\sqrt{\frac{N}{|M|}}}(\frac{\theta'}{2})}. \tag{S22}$$

When viewed from sphere surface, as shown in Fig. S1(b), the equivalent refractive index profiles $|n|$ at θ'=0, π/2, π are infinite, 1, and infinite respectively. Therefore, light from the equator is gradually caught into the north and south poles, which looks like two black holes setted there.

Section 4: Permittivity transformation in different coordinate systems

In order to facilitate simulation and calculation, we need to transform the permittivity in curved coordinate system to the permittivity in Cartesian coordinate system (x, y, z) by the transformation optics,

$$\varepsilon_{xyz} = \frac{\hat{J}\varepsilon_{\text{curved}}\hat{J}^T}{\left|\det(\hat{J})\right|}, \tag{S23}$$

where $\hat{J} = \begin{bmatrix} \frac{\partial x}{\partial q_1} & \frac{\partial x}{\partial q_2} & \frac{\partial x}{\partial q_3} \\ \frac{\partial y}{\partial q_1} & \frac{\partial y}{\partial q_2} & \frac{\partial y}{\partial q_3} \\ \frac{\partial z}{\partial q_1} & \frac{\partial z}{\partial q_2} & \frac{\partial z}{\partial q_3} \end{bmatrix}$ is the Jacobian transformation matrix.

In the case of cylindrical coordinate, $\hat{J}(\varphi) = \begin{bmatrix} \cos(\varphi) & -\sin(\varphi) & 0 \\ \sin(\varphi) & \cos(\varphi) & 0 \\ 0 & 0 & 1 \end{bmatrix}$. So

$$\begin{aligned} \varepsilon_{xyz} &= \hat{J}(\varphi)\begin{bmatrix} \varepsilon_{\rho\rho} & 0 & 0 \\ 0 & \varepsilon_{\varphi\varphi} & 0 \\ 0 & 0 & \varepsilon_{zz} \end{bmatrix}\hat{J}^T(\varphi) \\ &= \begin{bmatrix} \varepsilon_{\rho\rho}\cos^2(\varphi)+\varepsilon_{\varphi\varphi}\sin^2(\varphi) & (\varepsilon_{\rho\rho}-\varepsilon_{\varphi\varphi})\sin(\varphi)\cos(\varphi) & 0 \\ (\varepsilon_{\rho\rho}-\varepsilon_{\varphi\varphi})\sin(\varphi)\cos(\varphi) & \varepsilon_{\varphi\varphi}\cos^2(\varphi)+\varepsilon_{\rho\rho}\sin^2(\varphi) & 0 \\ 0 & 0 & \varepsilon_{zz} \end{bmatrix}. \end{aligned} \tag{S24}$$

In the case of spherical coordinate, $\hat{J}(\theta,\varphi) = \begin{bmatrix} \sin(\theta)\cos(\varphi) & \cos(\theta)\cos(\varphi) & -\sin(\varphi) \\ \sin(\theta)\sin(\varphi) & \cos(\theta)\sin(\varphi) & \cos(\varphi) \\ \cos(\theta) & -\sin(\theta) & 0 \end{bmatrix}$. So

$$\begin{aligned} \varepsilon_{xyz} &= \hat{J}(\theta,\varphi)\begin{bmatrix} \varepsilon_{rr} & 0 & 0 \\ 0 & \varepsilon_{\theta\theta} & 0 \\ 0 & 0 & \varepsilon_{\varphi\varphi} \end{bmatrix}\hat{J}^T(\theta,\varphi) \\ &= \begin{bmatrix} (\varepsilon_{rr}\sin^2(\theta)+\varepsilon_{\theta\theta}\cos^2(\theta))\cos^2(\varphi)+\varepsilon_{\varphi\varphi}\sin^2(\varphi) & (\varepsilon_{rr}\sin^2(\theta)+\varepsilon_{\theta\theta}\cos^2(\theta)-\varepsilon_{\varphi\varphi})\sin(\varphi)\cos(\varphi) & (\varepsilon_{rr}-\varepsilon_{\theta\theta})\sin(\theta)\cos(\theta)\cos(\varphi) \\ (\varepsilon_{rr}\sin^2(\theta)+\varepsilon_{\theta\theta}\cos^2(\theta)-\varepsilon_{\varphi\varphi})\sin(\varphi)\cos(\varphi)) & (\varepsilon_{rr}\sin^2(\theta)+\varepsilon_{\theta\theta}\cos^2(\theta))\sin^2(\varphi)+\varepsilon_{\varphi\varphi}\cos^2(\varphi) & (\varepsilon_{rr}-\varepsilon_{\theta\theta})\sin(\theta)\cos(\theta)\sin(\varphi) \\ (\varepsilon_{rr}-\varepsilon_{\theta\theta})\sin(\theta)\cos(\theta)\cos(\varphi) & (\varepsilon_{rr}-\varepsilon_{\theta\theta})\sin(\theta)\cos(\theta)\sin(\varphi) & \varepsilon_{rr}\cos^2(\theta)+\varepsilon_{\theta\theta}\sin^2(\theta) \end{bmatrix}. \end{aligned} \tag{S25}$$

Section 5: The hyperbolic ray and field response to the dipoles at other positions

In order to explore the light response to the dipole incident from the other points on the spherical surface, we change the position of the electric pole to point (θ, φ) = (π/3,0) when other settings are the same as in Fig. 5. According to geodesic equation Eq. (S7) and finite element method, the results of ray and electric field E_r are shown in Fig. S2. Because the sphere is highly symmetrical, the result is representative.

As shown in Fig. S2, the light would still focus on the north and south poles of the sphere influenced by the ultra refractive index on the poles. Differently, the hyperbolic wavefront area above the dipole is much smaller than that below the dipole because the movement of the dipole breaks the propagation symmetry of the hyperbolic branch.

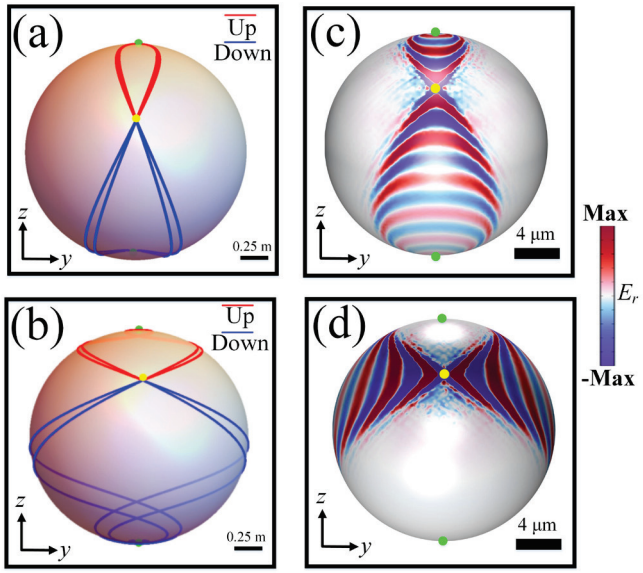

Fig. S2 Geodesics on the spherical surface for hyperbolic anisotropic coefficients **(a)** M = 1, N = -4 and **(b)** M = -4, N = 1. The electric field E_r for hyperbolic anisotropic permittivity **(c)** ε_θ =-4.04-0.34i, ε_φ=1.02-0.07i and **(d)** ε_θ =1.02-0.07i, ε_φ=-4.04-0.34i. The yellow points are the sources and the green points are images.

Section 6: Metastructure realization of curved hyperbolic polaritons

In addition to the realization based on the two-dimensional van der Waals films in Fig. 5, other design possibilities can also be considered. For example, moiré metastructures based on graphene can be constructed to support the highly confined hyperbolic polaritons in the infrared band [Ref. [34] in the main text]. Here, we design a parallel nanowire array structure consisting of spherical symmetric graphene films, as shown in Fig. S3(a). Curved graphene films can be either fabricated by transferring graphene onto curved dielectric substrates or grown directly by laser ablation on the structured surface of SiC demonstrated recently [S5]. In addition, creating pressure difference (ΔP) between the inside and outside of the suspended graphene membrane can control the shape of suspended graphene [Ref. [38] in the main text]. We define the filling factor of Graphene from $\eta = d_1/(d_1 + d_2)$, where d_1 and d_2 are the width of Graphene film and void. The incident wavelength and the Fermi energy are set as λ=11.05 μm and E_F= 0.075 ev, so the permittivity of Graphene films is ε_g= -29.65-2.45i which can be obtained using Kubo formula [S6]. Here we set η= 0.5. With the help of the effective medium theory [S2],

$$\varepsilon_\theta = \eta\varepsilon_1 + (1-\eta)\varepsilon_2,$$
$$\varepsilon_\varphi = \frac{(1+\eta)\varepsilon_1\varepsilon_2 + (1-\eta)\varepsilon_2^2}{(1+\eta)\varepsilon_2 + (1-\eta)\varepsilon_1}, \quad \text{(S26)}$$

the equivalent in-plane permittivity of the metastructures can be calculated as ε_θ=-14.33-1.23i, ε_φ=3.3-0.03i, respectively. When constructing an elliptic anisotropic metastructures, there is a restriction $|\alpha^2| > 1$, but this restriction does not apply when we construct the designed hyperbolic metastructures. Using the same excitation method, the electric field distribution E_r based on metastructures shows the same focusing properties as that of the natural hyperbolic material (see Figs. S3(b)), which verifies the possibility of our metastructure realization.

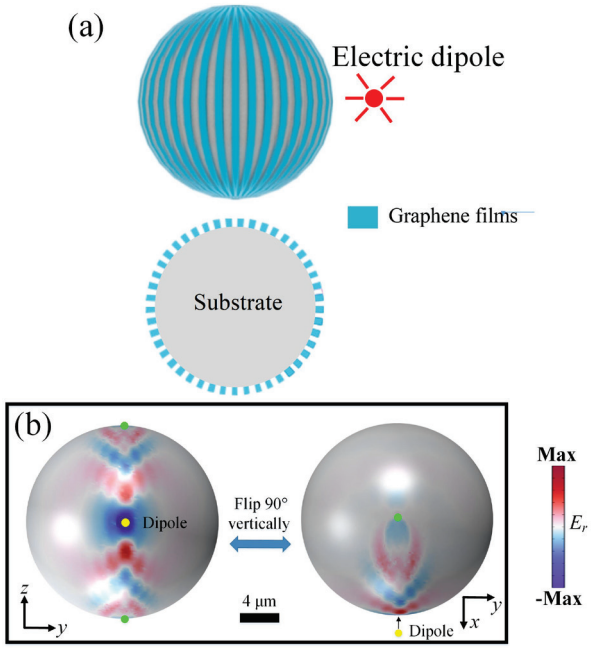

Fig. S3 (a) The metastructure realization of spherical hyperbolic anisotropies based on Graphene films. The incident wavelength and the Fermi energy are set as λ=11.05 μm and E_F= 0.075 eV. **(b)** The electric field E_r on the surface of the metastructure. The yellow points are the sources and the green points are images.

References

S1. H. Goldstein, C. Poole, and J. Safko, Classical Mechanics, 3rd Ed., Addison Wesley, Reading, MA, 2001

S2. Y. L. Zhang, J. B. Pendry, and D. Y. Lei, Radial anisotropy from a geometric viewpoint: Topological singularity and effective medium realization, *Phys. Rev. B* 96(3), 3035430 (2017)

S3. I. I. Smolyaninov, E. Hwang, and E. Narimanov, Hyperbolic metamaterial interfaces: Hawking radiation from Rindler horizons and spacetime signature transitions, *Phys. Rev. B* 85(23), 235122 (2012)

S4. S. Tao, W. Xiao, and H. Chen, Light behaviors outside a black hole surrounded by dark matter, *EPL* 136(1), 14002(2022)

S5 L. Gerhard, E. Moyen, T. Balashov, I. Ozerov, M. Portail, H. Sahaf, L. Masson, W. Wulfhekel, and M. Hanbücken, A graphene electron lens, *Appl. Phys. Lett.* 100(15), 153106 (2012)

S6. P. Y. Chen and A. Alu, Atomically thin surface cloak using graphene Monolayers, *ACS Nano* 5, 5855 (2011)